27 July 2026

CO Adsorption on MgO Revisited: Polarization-Resolved Identification of Step Edges as the Dominant Defects on MgO(100) and MgO(110)

Wangtao Li[1], Chengwu Yang[2], Pablo G. Lustemberg[3], Zairan Yu[1], Alexei Nefedov[1], Weijia Wang[1], Gianfranco Pacchioni[4], M. Veronica Ganduglia-Pirovano[3], Yuemin Wang[1], Christof Wöll[1,5]

1. Institute of Functional Interfaces (IFG, Karlsruhe Institute of Technology (KIT
2. Institute of Coal Chemistry, Chinese Academy of Sciences
3. Institute of Catalysis and Petrochemistry (ICP, Spanish National Research Council (CSIC
4. Dipartimento di Scienza dei Materiali, Università Milano-Bicocca
5. Ordos Laboratory

Abstract

Magnesium oxide is a paradigmatic ionic oxide, yet its experimentally observed chemical activity remains difficult to reconcile with its wide band gap and non-reducible character. Here, we combine polarization-dependent infrared reflection–absorption spectroscopy with hybrid density functional theory to investigate CO adsorption on welldefined MgO single-crystal surfaces, explicitly disentangling the roles of surface orientation, point defects, and low-coordination step-edge sites. Using CO as a site-sensitive vibrational probe, we demonstrate that the reactivity of MgO(100) originates from fourfold-coordinated Mg_{4c}^{2+} step-edge sites rather than terrace Schottky defects. Distinct vibrational signatures, adsorption geometries, and binding energies are observed in quantitative agreement between experiment and theory. On the more open MgO(110) surface, where Mg_{4c}^{2+} sites are intrinsic to the terrace, a coordination-controlled trend emerges: Mg_{4c}^{2+} sites bind CO more strongly and exhibit higher-frequency bands than Mg_{5c}^{2+} sites. Analysis of transition dipole moments further reveals a substantial enhancement of infrared intensities at low-coordinated sites, underscoring the need to account for site-specific dipole strengths in spectral interpretation. These results establish extended low-coordination motifs as the dominant defect sites on MgO surfaces, with direct implications for metal anchoring and the design of defect-engineered oxide catalysts.

Keywords

Active Sites • DFT, IRRAS • Magnesium Oxide • Schottky Defects • Step Edges

CO Adsorption on MgO Revisited: Polarization-Resolved Identification of Step Edges as the Dominant Defects on MgO(100) and MgO(110)

Wangtao Li,[a,§] Chengwu Yang,[b,§] Pablo G. Lustemberg,[c,§] Zairan Yu,[a] Alexei Nefedov,[a] Weijia Wang,[a] Gianfranco Pacchioni,[d] M. Veronica Ganduglia-Pirovano,[c,*] Yuemin Wang,[a,*] and Christof Wöll [a,e*]

[a] Institute of Functional Interfaces (IFG), Karlsruhe Institute of Technology (KIT), 76344 Eggenstein-Leopoldshafen, Germany

[b] Institute of Coal Chemistry, Chinese Academy of Sciences, 030001 Taiyuan, China

[c] Institute of Catalysis and Petrochemistry (ICP), Spanish National Research Council (CSIC), 28049 Madrid, Spain

[d] Dipartimento di Scienza dei Materiali, Università Milano-Bicocca, 20125 Milano, Italy

[e] Ordos Laboratory, Ordos, Inner Mongolia 017010, China

[§] These authors contributed equally to this work.

*Corresponding authors: yuemin.wang@kit.edu; christof.woell@kit.edu; vgp@icp.csic.es

ABSTRACT: Magnesium oxide is a paradigmatic ionic oxide, yet its experimentally observed chemical activity remains difficult to reconcile with its wide band gap and non-reducible character. Here, we combine polarization-dependent infrared reflection–absorption spectroscopy with hybrid density functional theory to investigate CO adsorption on well-defined MgO single-crystal surfaces, explicitly disentangling the roles of surface orientation, point defects, and low-coordination step-edge sites. Using CO as a site-sensitive vibrational probe, we demonstrate that the reactivity of MgO(100) originates from fourfold-coordinated Mg_{4c}^{2+} step-edge sites rather than terrace Schottky defects. Distinct vibrational signatures, adsorption geometries, and binding energies are observed in quantitative agreement between experiment and theory. On the more open MgO(110) surface, where Mg_{4c}^{2+} sites are intrinsic to the terrace, a coordination-controlled trend emerges: Mg_{4c}^{2+} sites bind CO more strongly and exhibit higher-frequency bands than Mg_{5c}^{2+} sites. Analysis of transition dipole moments further reveals a substantial enhancement of infrared intensities at low-coordinated sites, underscoring the need to account for site-specific dipole strengths in spectral interpretation. These results establish extended low-coordination motifs as the dominant defect sites on MgO surfaces, with direct implications for metal anchoring and the design of defect-engineered oxide catalysts.

Keywords: Active Sites • DFT, IRRAS • Magnesium Oxide • Schottky Defects • Step Edges

TOC GRAPHIC

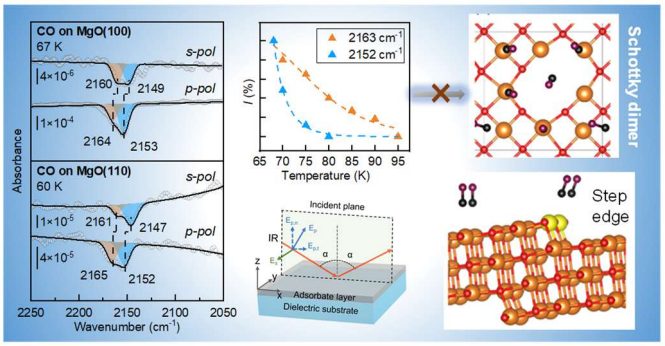

By combining polarization-resolved IRRAS with hybrid HSE06 DFT calculations, we establish site-specific vibrational fingerprints, adsorption geometries, and binding energies for CO on wide-band-gap MgO surfaces. Low-coordinated Mg_{4c}^{2+} step-edge sites, rather than terrace Schottky defects, are identified as the dominant binding and reactive sites, with direct implications for defect-engineered oxides and oxide-supported single-atom catalysis.

1. Introduction

Magnesium oxide is a wide-band-gap, nonreducible oxide that has long served as a benchmark system for studying weak adsorption on insulating surfaces. Achieving quantitative agreement between experiment and theory—even for an ostensibly "simple" adsorbate such as CO on MgO(100)—has nevertheless required substantial effort.[1] Based on its closed-shell electronic structure and large band gap, the ideal MgO(100) terrace is generally expected to be chemically inert. Yet, this expectation contrasts sharply with the excellent catalytic performance exhibited by MgO in organic transformations such as the dehydrogenation of secondary aliphatic alcohols[2] and transfer hydrogenation.[3] Numerous experimental studies have reported pronounced, site-specific reactivity on MgO surfaces, manifested by enhanced adsorption energies and substantial vibrational frequency shifts of small adsorbates.[4] This apparent contradiction, often referred to as the MgO chemical activity paradox, reflects a fundamental gap between the idealized terrace model and the behavior of real surfaces and is commonly attributed to low-coordination sites such as vacancies (F centers and Schottky defects), step edges, and kinks, which generate local electrostatic fields capable of stabilizing directional adsorbate–surface interactions without invoking bulk reducibility or cation redox chemistry.[5]

Despite their recognized importance, the spectroscopic signatures and adsorption energetics of individual defect types on this prototypical ionic surface remain poorly defined. In particular, the relative contributions of terrace defects versus extended step structures to the observed reactivity have not been resolved experimentally. Identifying reactive sites on MgO surfaces therefore requires site-resolved information on interactions with probe molecules such as CO—an approach that is also applicable under operando conditions.[6]

Here, we address this challenge by providing a direct, site-resolved spectroscopic characterization of CO adsorbed on MgO(100) and MgO(110) single-crystal surfaces, including experimentally determined binding energies. By combining polarization-dependent infrared reflection–absorption spectroscopy (IRRAS), density-functional theory (DFT) calculations, and the deliberate preparation of surfaces with varied step abundance, we determine the adsorption geometry, vibrational fingerprint, binding energetics and coverage dependence of CO at differently coordinated Mg^{2+} sites. Notably, investigation of the previously unexplored (110) surface reveals a scenario distinct from MgO(100), in which CO bound to step defects exhibits a lower vibrational frequency than CO adsorbed on regular terrace sites.

The adsorption energies obtained experimentally are incompatible with CO bound to terrace color centers or Schottky defects. Instead, step edges are identified as the predominant defects on these two low-Miller-index MgO surfaces. Crucially, quantification of site-dependent transition dipole moments (TDM) reveals that the infrared intensities associated with step-edge-bound CO exceed those of terrace species by approximately a factor of five. This finding demonstrates that the absence of site-resolved information can lead to substantial misinterpretation of infrared spectra. Together, these results have direct implications for metal anchoring and the rational design of MgO-supported species, particularly single-atom catalysts.[7]

2. Results and Discussion

Previous low-temperature IR spectroscopic studies of CO adsorption on MgO(100) surfaces have consistently reported a dominant vibrational band centered at ~ 2152 cm^{-1} (Figure S1a-c).[1f-i] For cleaved MgO(100) single crystals, Heidberg et al. observed exclusively this feature, with no indication of higher-frequency components.[1f] In these early measurements, IR spectra were recorded in transmission geometry, and the sensitivity was insufficient to detect the CO band in s-polarization. Similarly, MgO smoke particles with well-defined cubic morphology, exposing predominantly (100) facets, exhibited only the 2152 cm^{-1} band.[1g] For more defective particles, a weak band at ~ 2165 cm^{-1} was attributed to CO bound to Mg cations at edges,[8] as also reported by Sterrer et al. for CO adsorbed on thin MgO(100) films (≈20 monolayers) grown on Mo(001) substrates.[1h, 1i] Polarization-dependent measurements were not feasible in these previous studies: for powder samples they are inherently inaccessible, and for metal-supported thin films the surface selection rule precludes measurements with s-polarization. Moreover, experimental data for CO bound to MgO(110) surfaces are not available to date.

Figure 1a shows deconvoluted p-polarized IRRAS spectra of CO adsorbed on sputter-annealed macroscopic MgO(100) single crystals at 67 K. The surface quality was assessed by grazing-emission X-ray photoelectron spectroscopy (XPS) and low-energy electron diffraction (LEED). The XPS data reveal a chemically clean surface containing only trace amounts of Ca^{2+} impurities (0.3 ± 0.2%, Figure S2a). A detailed analysis of the XPS information depth and upper limit of the surface Ca concentration is provided in the Supporting Information. The LEED data confirms (1x1) ordered surface structure with no evidence of Ca-induced reconstruction (Figure

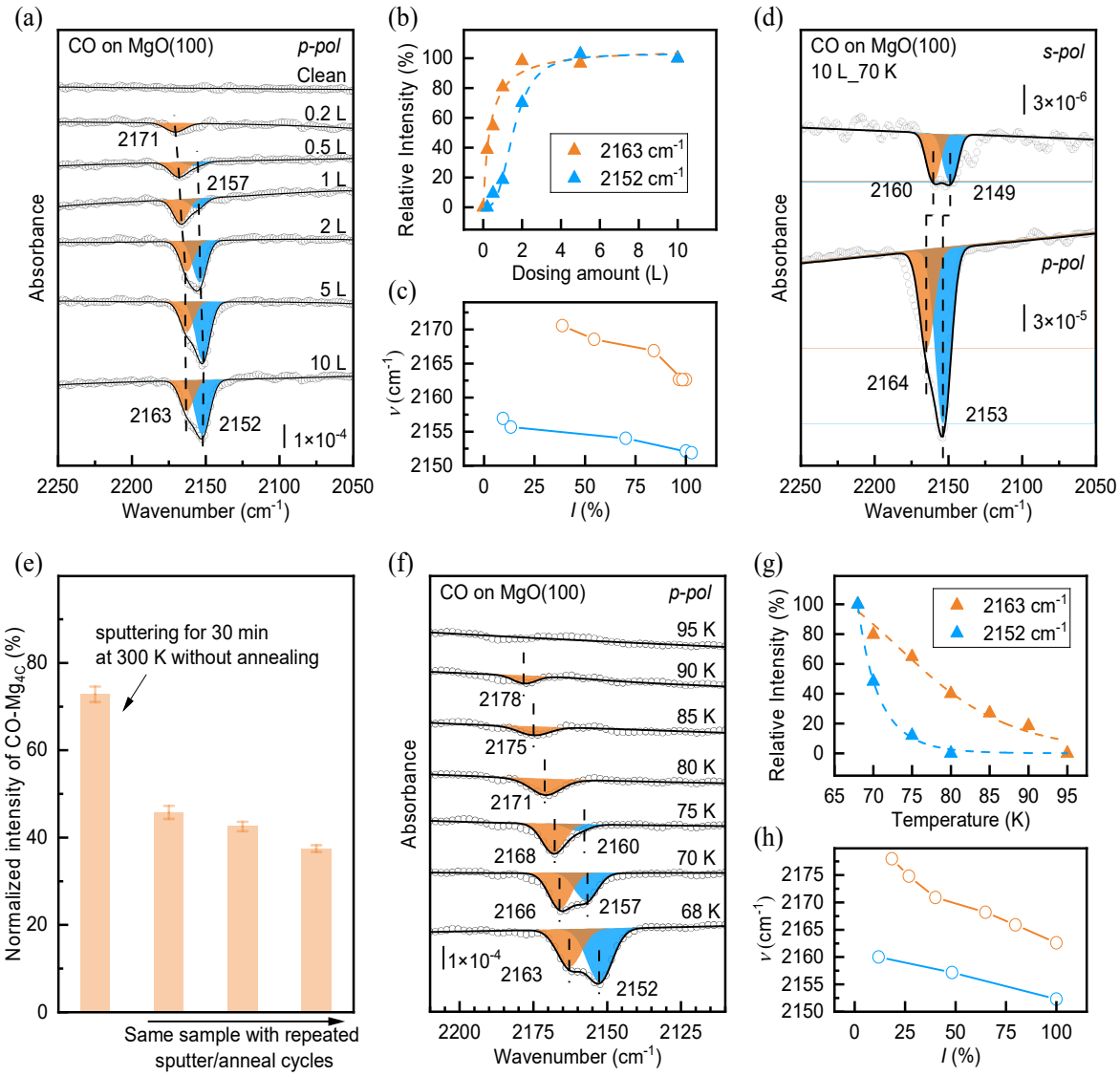

Figure 1. Polarization-resolved IRRAS data for CO adsorption on MgO(100) single crystal surfaces. (a) Deconvoluted coverage-dependent IRRAS spectra recorded with *p*- polarized light at 67 K. (b) Integrated intensities of the CO bands as a function of CO dose. (c) Vibrational frequency shifts of the two CO bands as a function of relative band intensity. (d) Deconvoluted *p*- and *s*-polarized IRRAS spectra acquired after CO exposure (10 L) on MgO(100) at 70 K. (e) Relative intensity of the defect-related high-frequency CO band (~2165 cm^{-1}), defined as the ratio of the peak area of the 2165 cm^{-1} band to the total peak area of both CO bands, as a function of surface preparation by successive sputtering (10 min at 300 K) and annealing (15 min at 850 K in 1 × 10^{-6} mbar O_2) cycles. (f-h) Temperature-dependent IRRAS data for CO desorption from MgO(100): (f) Deconvoluted *p*-polarized IRRAS data recorded after CO adsorption (10 L) at 68 K and subsequent annealing to the indicated temperatures. (g) Integrated intensities of the CO bands associated with Mg_{5c}^{2+} terrace sites and Mg_{4c}^{2+} defect sites as a function of sample temperature, used for Redhead-type analysis of adsorption energies. (h) Vibrational frequency shifts of the CO bands as a function of relative band intensity during the desorption process. All spectra were measured at a grazing incidence angle of 80° under UHV conditions (base pressure 8 × 10^{-11} mbar).

S2b).[9] Importantly, the LEED pattern exhibits broadened diffraction spots, indicating a significant density of surface defects on MgO(100), as corroborated by the corresponding IRRAS data.

At low coverage, a single high-frequency band at 2171 cm^{-1} is observed, gradually red-shifting with increasing CO dose (Figure 1b, c). As this band approaches saturation, a second feature at 2157 cm^{-1} emerges and becomes dominant. At saturation, alongside the main band at 2152 cm^{-1} assigned to CO adsorbed on five-fold coordinated Mg_{5c}^{2+} terrace sites, a distinct blue-shifted peak is unambiguously identified at 2163 cm^{-1}.

A key difference between these two CO species is revealed by the polarization-resolved spectra in Figure 1d. While the 2164 cm^{-1} band is significantly weaker than the 2153 cm^{-1} band in p-polarization, the two bands exhibit comparable intensities in s-polarization (intensity ratio ≈ 1:1 in s-polarized versus ~1:2 in p-polarized). This observation indicates a predominantly upright adsorption geometry for the 2153 cm^{-1} species, with only a small apparent tilt arising from thermally excited librations.[10] In contrast, the increased relative intensity of the 2164 cm^{-1} band in s-polarization reflects a substantially tilted adsorption geometry. We note that the small frequency splitting (~4 cm^{-1}) between p- and s-polarized spectra arises from the dielectric response of the substrate and is intrinsic to IRRAS on insulating surfaces.[10]

The evolution of the CO-IRRAS data upon systematic modification of the MgO(100) surface further supports the assignment of the high-frequency CO band to adsorption at defect-related sites (Figure S3). Successive sputter-anneal cycles lead to a gradual decrease in the relative intensity of the ~2165 cm^{-1} band (Figure 1e), consistent with a reduction in the density of low-coordination defect sites upon high-temperature annealing. In contrast, sputtering at 300 K for 30 min without subsequent annealing produces a markedly enhanced contribution of the high-frequency feature, which accounts for approximately 73% of the total CO signal. Together, these results support the assignment of the 2165 cm^{-1} band to CO adsorbed at low-coordinated Mg_{4c}^{2+} surface defects. We note, however, that the relative IRRAS intensities of terrace- and defect-related CO bands cannot be interpreted directly in terms of the relative occupation of the corresponding adsorption sites, because the measured intensities also depend on adsorption geometry, polarization selection rules, coverage, and the site-dependent transition dipole moment (TDM).[11] As discussed below, DFT calculations show that the IR intensity associated with the CO stretching mode is larger for CO adsorbed at step-related sites than for CO adsorbed on terrace sites.

Temperature-dependent IRRAS measurements provide direct information on the binding energies of the distinct CO species on MgO(100). Figure 1f shows deconvoluted p-polarized IRRAS spectra recorded during annealing of the CO-covered surface. With increasing temperature, the 2152 cm-1 band assigned to CO adsorbed on Mg_{5c}^{2+} terrace sites on MgO(100) rapidly attenuates and disappears at ~75 K. In contrast, the high-frequency CO signal associated with defect-related Mg_{4c}^{2+} sites persists to higher temperatures and vanishes only after heating to ~95 K. A Redhead-type analysis[12] (Figure 1g) yields adsorption energies of 21.5 kJ mol^{-1} (0.22 eV) for CO bound to Mg_{5c}^{2+} terrace sites and 27.5 kJ mol^{-1} (0.28 eV) for CO adsorbed at Mg_{4c}^{2+} defect sites in the low-coverage limit, corresponding to isolated CO at the respective sites. The CO binding energy on regular Mg_{5c}^{2+} sites agrees well with values reported from temperature-programmed desorption experiments (20.6 ± 2.4 kJ mol^{-1})[1n] and DFT calculations (21.2 kJ mol^{-1}).[13] For CO at Mg_{4c}^{2+} steps, a comparable binding energy of 0.33 eV was reported from Hartree-Fock cluster model calculations.[14]

In addition to changes in intensity, all CO adsorbate species on MgO(100) exhibit systematic blue shifts in their vibrational frequencies as the coverage decreases during annealing (Figure 1h). For CO–Mg_{5c}^{2+}, the band maximum shifts from 2152 to 2161 cm^{-1}, while the CO–Mg_{4c}^{2+} band shifts from 2163 to 2178 cm^{-1}. Similar coverage-dependent frequency shifts are observed during CO adsorption at 67 K (see Figure 1c) and are attributed to repulsive lateral interactions between adsorbed CO molecules, arising from a combination of dynamic dipole-dipole coupling and substrate-mediated static interactions.[15]

Interestingly, the more open MgO(110) surface exhibits markedly different CO adsorption behavior. The surface quality was characterized by grazing-emission XPS and LEED (Figure S4). XPS analysis again reveals only trace amounts of Ca^{2+} (0.8 ± 0.2 %) (Figure S4b) A detailed analysis of the XPS information depth and upper limit of the surface Ca concentration is provided in the Supporting Information. The LEED data shows no evidence of Ca-induced reconstruction (Figure S4b).[9] Notably, the LEED pattern exhibits weak diffuse streaking, indicative of {100}-type surface faceting,[16] fully consistent with the IRRAS observations discussed below.

Figure 2 shows the deconvoluted, polarization-resolved IRRAS spectra at 60 K. In p-polarization (Figure 2a), the dominant CO band appears at 2175 cm^{-1} at low coverage and shifts to 2165 cm^{-1} at saturation, consistent with adsorption on regular fourfold-coordinated Mg_{4c}^{2+}

terrace sites. Its absence or weak intensity in s-polarization (Figure 2b) indicates a nearly upright geometry. A second band at 2158–2153 cm^{-1} in p-polarization can be assigned to CO on fivefold-coordinated Mg_{5c}^{2+} ions at step sites; its predominance in s-polarization confirms a tilted geometry (Figure S5). We note that CO signals measured with s-polarized light are intrinsically much weaker than those observed in the p-polarized spectra, rendering the corresponding IRRAS measurements substantially more challenging.[11]

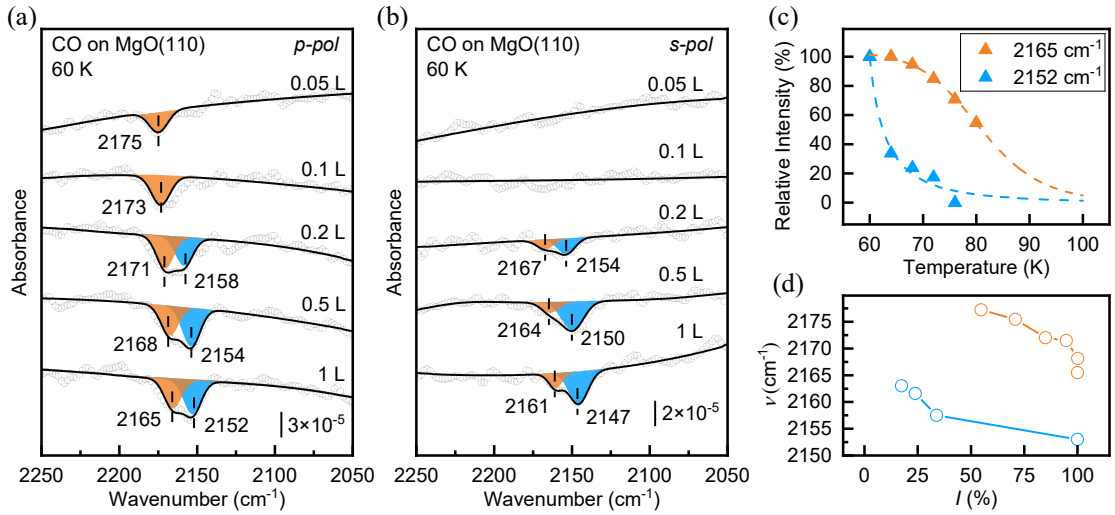

Figure 2. (a,b) Deconvoluted polarization-resolved IRRAS data for CO adsorption on MgO(110) at 60 K as a function of CO dose: (a) p-polarized IRRAS spectra; (b) s-polarized IRRAS spectra. (c,d) Temperature-dependent IRRAS data for CO desorption from MgO(110) recorded after CO adsorption (1 L) at 60 K and subsequent annealing to the indicated temperatures. (c) Integrated intensities of the distinct CO bands as a function of sample temperature, used for Redhead-type analysis of adsorption energies. (d) Vibrational frequency shifts of the CO bands as a function of relative band intensity during the desorption process. All spectra were collected at a grazing incidence angle of 80° along the [001] azimuth. The small frequency offset (~4 cm^{-1}) between s- and p-polarized spectra arises from the dielectric response of the substrate and is intrinsic to IRRAS on insulating surfaces.[10]

Temperature-dependent spectral analysis (Figure 2c, Figure S6) yields binding energies of 21.5 kJ mol^{-1} (0.22 eV) for CO on Mg_{5c}^{2+} and 28.0 kJ mol^{-1} (0.29 eV) for CO on Mg_{4c}^{2+}, in line with values on MgO(100). Furthermore, similar coverage-related frequency shifts are observed for both CO species during adsorption (Figure 2a, b) and desorption (Figure 2d). Such coverage-induced frequency shifts are not expected for isolated defects, such as terrace vacancies and color centers, or for randomly distributed step and kink sites. Overall, these observations in CO vibrational frequency, adsorption geometry, and binding energy provide further evidence that

the 2163 cm^{-1} band on MgO(100) originates from CO bound to fourfold-coordinated Mg_{4c}^{2+} defect sites.

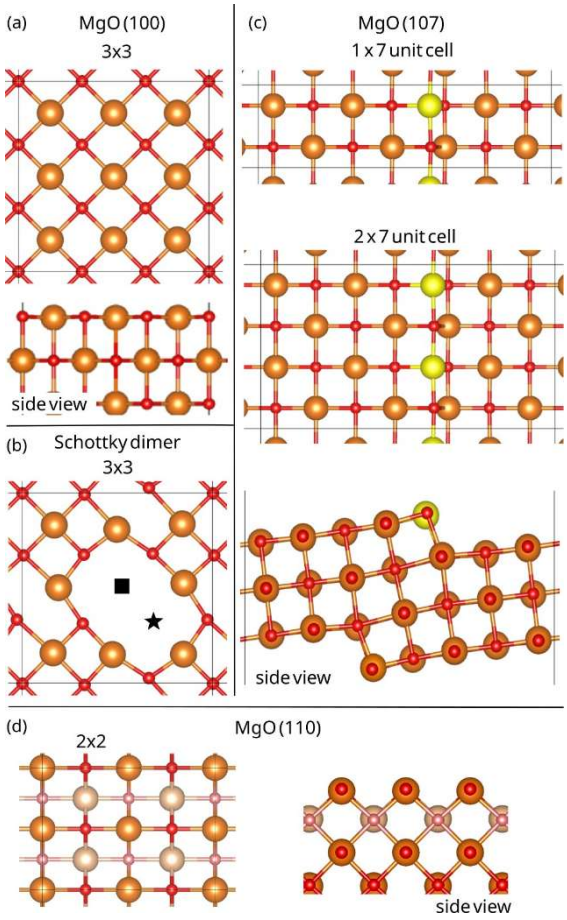

Figure 3. Surface models employed in the DFT calculations. (a) Pristine MgO(100) terrace represented by a slab model using a (3×3) supercell (top and side views). (b) MgO(100) slab with (3×3) surface periodicity containing a Schottky dimer defect, consisting of adjacent Mg and O vacancies (top view). (c) Stoichiometric MgO(107) stepped slabs exposing monoatomic step edges, shown for (1×7) and (2×7) surface supercells (top views). (d) Stoichiometric MgO(110) surface (top and side views). For clarity, the top views in (a) and (d) display only the outermost surface layer of the slab. Color code: fivefold-coordinated surface Mg (Mg_{5c}) in orange, fourfold-coordinated Mg (Mg_{4c}, characteristic of step-edge sites) in yellow, and O in red. For the MgO(110) model in (d), Mg and O atoms in the second layer are displayed in lighter shades to distinguish them from the outermost surface layer. Mg vacancies are indicated by black squares and O vacancies by black stars. This color scheme is used consistently throughout all figures in this paper.

To interpret the polarization-dependent IRRAS results and establish an unambiguous adsorption-site assignment, density functional theory (DFT) calculations were performed for

CO on MgO. Three model systems were considered (Figure 3): (i) the ideal MgO(100) terrace, represented by a slab model using a (3×3) surface supercell; (ii) the lowest-energy terrace point defect examined here, an adjacent Mg–O vacancy pair ("Schottky dimer") within the same (3×3) surface supercell; and (iii) monoatomic step edges modeled using stoichiometric MgO(107) stepped slabs with a (1×7) surface repeat unit. The complete set of pristine, point-defect, and extended-defect models screened in this work, together with their defect-formation energies, is shown in Figure S7. A larger (2×7) surface supercell was employed to assess convergence with respect to adsorbate–adsorbate interactions along the step edge. A wider set of point and extended defects (including O and Mg vacancies and Frenkel-type motifs) was screened; these structures are substantially less stable than the Schottky dimer and are therefore not expected to dominate the defect population under our preparation conditions. The corresponding structures, formation energies, and computational settings are reported in the Supporting Information. For each of the three target models, we computed adsorption energies, optimized geometries (including the CO tilt angle), harmonic C–O stretching frequencies, and infrared intensities (proportional to the square of the transition dipole moment), enabling a direct comparison with the experimentally determined binding energies, vibrational shifts, and polarization-dependent intensities.

A long-standing issue in the CO/MgO literature is that absolute adsorption energies are sensitive to the electronic-structure treatment and computational details, reflecting the largely electrostatic nature of CO binding on MgO(100). Early periodic calculations comparing Hartree-Fock and local density functional descriptions already highlighted this method dependence.[1e] High-level benchmarks based on correlated wavefunction methods have since converged on low-coverage adsorption energies on the order of ~20 kJ mol^{-1}.[1q, 1r, 13] Other studies pointed to the relevant role of dispersion contributions.[17] The current view is that of weak physisorption largely governed by electrostatics and polarization, with a secondary contribution from dispersion. Importantly, recent periodic correlated calculations explicitly spanning dilute to high-coverage regimes ($\Theta \rightarrow 1$) report that the binding strength becomes substantially less exothermic, reflecting the growth of lateral CO–CO repulsion.[18]

As described above, the temperature-dependent IRRAS data for MgO(100) (Figure 1f-h) show systematic blue shifts of both CO bands as their intensities decrease during desorption, directly evidencing repulsive lateral interactions within the adlayer. Complementary polarization-resolved dosing experiments on MgO(100) (Figure 1a-c) further reveal a clear coverage-dependent evolution of band positions and relative intensities. Although the integrated band

intensities approach saturation at higher exposures, the continued coverage-dependent spectral evolution indicates that the local adsorption environment does not converge to a single, coverage-independent vibrational signature characteristic of a well-defined commensurate monolayer (ML). Within this context, our objective is not to redefine a benchmark adsorption energy, but to employ an internally consistent dataset to assess whether the formation of a stable, homogeneous CO monolayer is thermodynamically compatible with the experimental regime.

To this end, we evaluated the coverage dependence of the adsorption strength on the MgO(100) terrace by computing the average CO adsorption energy per molecule ($|E_{ads/CO}|$) as a function of Θ (Figure 4a). This analysis was performed at the PBE level, enabling systematic treatment of multiple coverages and adlayer arrangements at manageable computational cost. This choice is further motivated by prior studies of CO adsorption on oxide surfaces showing that, for weakly bound CO, hybrid functionals (e.g., HSE06) yield adsorption energies on a comparable energy scale to GGA(+U) approaches,[19] even though vibrational properties exhibit greater functional sensitivity.

The computed trend in Figure 4a reveals a progressive reduction of $|E_{ads/CO}|$ with increasing Θ, with pronounced weakening toward high coverage. This behavior reflects increasingly repulsive lateral interactions within the CO adlayer, including dipole-dipole coupling and packing constraints. The energetic trend thus provides a thermodynamic explanation for the coverage-dependent spectral evolution observed experimentally.

Finally, the coverage dependence provides a natural link between adsorption energetics and the structural organization of the CO adlayer. Even for the well-characterized commensurate CO overlayer on MgO(100), combined modelling and vibrational analysis have indicated that upright (top) and tilted CO motifs can coexist within the same ordered layer (e.g., at $\Theta \approx 0.75$ ML).[20] Notably, the commensurate c(4×2) overlayer reported in Ref.[20] forms at low temperature and near-monolayer coverage, whereas under the present IRRAS conditions CO remains in the submonolayer regime and the spectra are interpreted without invoking long-range adlayer order. This precedent for mixed adsorption geometries supports the interpretation that, at experimentally relevant coverages, both upright and tilted configurations contribute to the measured vibrational response.

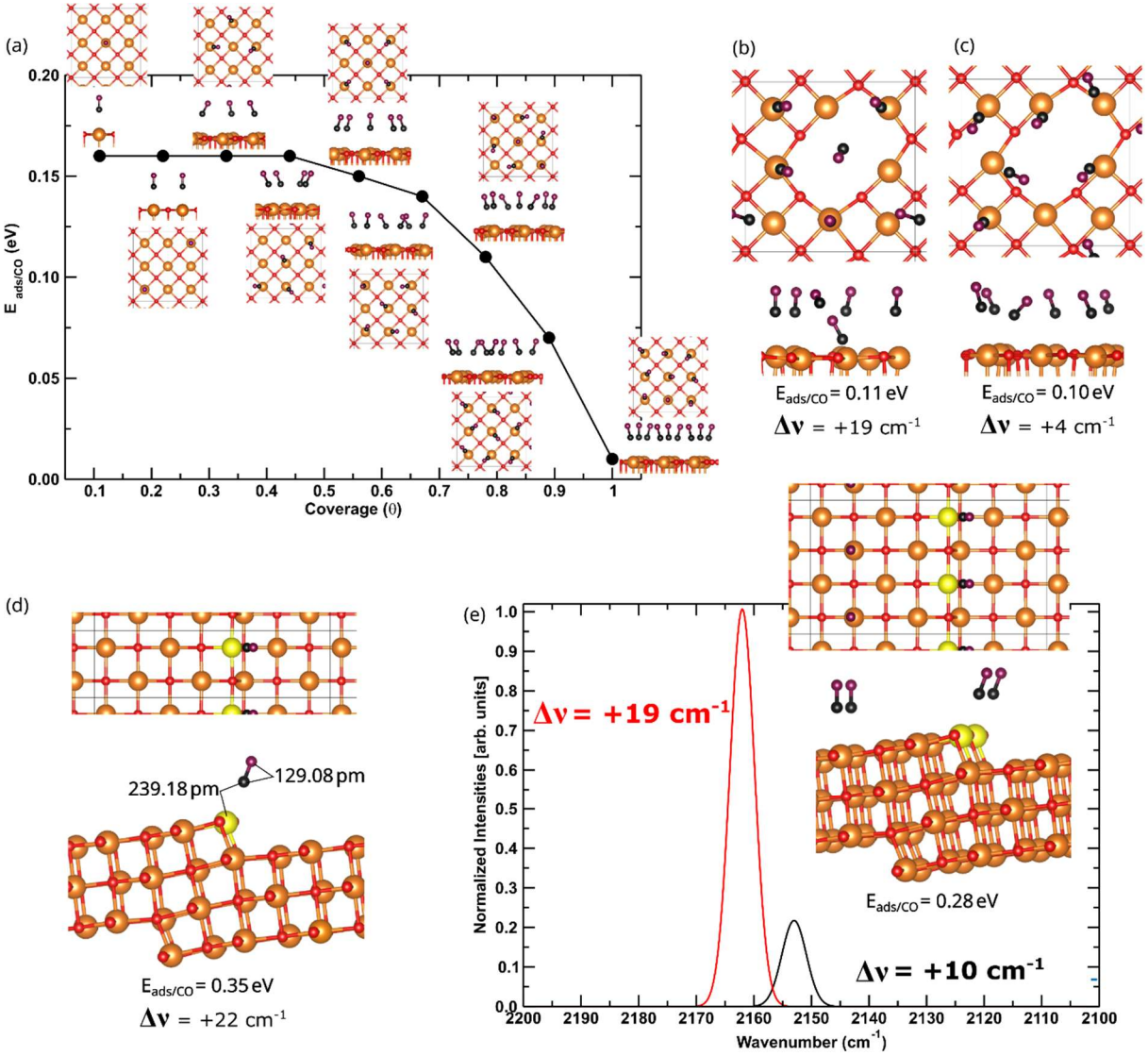

Figure 4. (a) Coverage dependence of the average adsorption energy per CO molecule, $|E_{ads/CO}|$, on MgO(100) computed at the PBE level; optimized structures corresponding to selected coverages are shown as insets (3×3 cell). (b, c) Top and side views of representative ordered CO adlayers on a Schottky dimer model at Θ = 2/3 ML, together with the computed adsorption energies ($E_{ads/CO}$) and C–O stretching-frequency shifts, Δν, relative to gas-phase CO. (d) Optimized geometry of a strongly bound CO species at an MgO step site, highlighting the Mg–C and C–O bond lengths and the corresponding $E_{ads/CO}$ and Δν (1×7 cell). (e) Simulated IR spectra for CO at step-edge (red) and terrace sites (black), illustrating the characteristic positive frequency shifts associated with step-edge and terrace adsorption configurations (2×7 cell). Adsorption energies and vibrational frequency shifts shown in panels (b–e) are computed at the HSE06 level. Color code: C atoms of CO are shown in black and O atoms of CO in violet.

To assess the microscopic origin of the experimentally observed terrace and defect-related CO bands, we directly compare the calculated adsorption properties of CO on the three MgO motifs introduced above. Among these, CO adsorption at Mg_{4c} step-edge sites stands out clearly. In the step-edge model, a single CO molecule bound to an Mg_{4c} cation exhibits a distinctly blue-shifted C–O stretching frequency ($\Delta\nu \approx +22$ cm^{-1}) together with a substantially stronger binding energy ($E_{ads/CO} \approx 0.35$ eV, Figure 4d). This combination of a sizeable positive frequency shift and enhanced adsorption strength matches closely the experimentally identified defect-related CO species, which persists to higher temperatures in the desorption series and is associated with the larger experimental binding energy (≈0.28 eV) of the defect-related CO band at 2163 cm^{-1}.

To further connect these energetic trends with the intensity analysis discussed above, we performed an ab initio thermodynamic comparison of selected CO-covered terrace, Schottky-defect, and step-edge configurations as a function of the CO chemical potential (Figure S8). This analysis is not intended to extract absolute coverages under the directional-dosing conditions of the experiment. Rather, it shows that step-bound CO configurations become stabilized at lower CO chemical potential than CO-covered terrace configurations, supporting the conclusion that equal fractional occupation of Mg_{4c}^{2+} step sites and Mg_{5c}^{2+} terrace sites is not expected under low-temperature submonolayer conditions.

A quantitative determination of the absolute defect density from IRRAS data is, however, not straightforward, because the intensity of an adsorbate vibration depends not only on the number of adsorbed molecules, but also on the fractional occupation of each site type, the site-specific CO-stretching response, and the adsorption geometry under polarization-resolved IRRAS conditions. In simplified form, the intensity of a band associated with site type i can be written as $I_i \propto N_i \theta_i A_i f_i$, where N_i is the number of available sites, θ_i their fractional CO occupation, A_i the calculated CO-stretching intensity, and f_i accounts for geometry- and polarization-dependent IRRAS effects. For the representative adsorption configuration considered here ($\theta_{step} = 1$ and $\theta_{terrace} = 0.33$ ML, Figure 4e), dynamic dipole contribution associated with the CO stretching mode is approximately five times larger for CO adsorbed at Mg_{4c}^{2+} step sites than for CO adsorbed at Mg_{5c}^{2+} terrace sites. Together with the stronger adsorption of CO at Mg_{4c}^{2+} step sites, this explains why the step-related band can remain comparatively intense despite the lower geometrical abundance of step sites, consistent with the experimentally observed intensity distribution discussed above.

Crucially, this assignment remains robust under conditions relevant to the experimental submonolayer regime. When a larger stepped surface cell (2×7) is populated with multiple CO

molecules, the calculations predict two step-related vibrational contributions centered at $\Delta\nu \approx +19$ and $+10$ cm^{-1}, with the $+19$ cm^{-1} component carrying the dominant computed infrared intensity (Figure 4e). This intensity hierarchy provides a direct explanation for why the experimentally observed defect band appears as a single dominant high-frequency feature rather than a clearly resolved doublet (Figure 1f): the IRRAS response is dominated by the step-associated mode with the larger transition dipole moment, while the weaker contribution would appear, at most, as a subtle shoulder.

For the Schottky-dimer model, we focused on an ordered multi-CO arrangement corresponding to a local coverage of $\Theta = 2/3$ ML, defined with respect to the available cationic adsorption sites in the defect-containing supercell (Figures 4b, c), where one Mg site is removed by the Schottky defect. This corresponds to a comparatively dense population of adsorption sites in the immediate defect environment. This choice is motivated by the preceding coverage analysis showing that, under the experimental submonolayer regime, CO is not expected to form a homogeneous close-packed layer; instead, locally dense patches can coexist with more weakly populated regions. Structurally, a Schottky dimer introduces low-coordination adsorption motifs (Mg_{4c}/O_{4c}) that are step-like in terms of reduced coordination. Importantly, even under this locally high-coverage condition, the Schottky model yields two distinct CO stretching contributions ($\Delta\nu \approx +4$ and $+19$ cm^{-1}) but significantly weaker adsorption energies ($E_{ads/CO} \approx 0.1$ eV), which are incompatible with the experimentally determined adsorption energy (~0.28 eV) of the defect-related CO band at 2163 cm^{-1}.

The thermodynamic propensity for generating extended step-like motifs is supported by the defect-formation energetics obtained from a (5×5) surface model. The formation energy of the first Schottky dimer, referenced to the defect-free surface, is 3.41 eV (Figure S8). Formation of two adjacent Schottky dimers requires 5.31 eV relative to the pristine surface, corresponding to an incremental formation energy of 1.90 eV for the second dimer. Thus, the incremental cost of creating a contiguous second dimer is reduced by approximately 45% compared with the first-dimer formation energy, indicating a driving force for defect aggregation. Such aggregation provides a structurally plausible route to extended vacancy or edge motifs with genuine step character, i.e., Mg4c environments consistent with the dominant experimental high-frequency CO band.

The polarization-dependent infrared intensity further reinforces the step-edge assignment when transition dipole moments are considered explicitly. The computed surface-normal CO-

stretching response for CO bound at Mg_{4c}^{2+} step-edge sites is larger than that for terrace-bound CO. This calculated enhancement should not be interpreted as a direct quantitative IRRAS intensity ratio, as the measured intensity also depends on fractional occupation, local step geometry, molecular orientation, coverage, and polarization conditions. Nevertheless, together with the stronger adsorption of CO at Mg_{4c}^{2+} sites and the polarization-resolved evidence for a tilted step-bound species, these results rationalize why the step-related band remains comparatively intense in the experimental spectra despite the lower concentration of step-edge sites relative to terrace sites. Taken together, the combined agreement in (i) adsorption strength, (ii) vibrational blue shift, and (iii) relative intensity supports the conclusion that the experimentally observed high-frequency CO band originates predominantly from CO bound at Mg_{4c} step-edge sites rather than from isolated Schottky-dimer motifs on the terrace.

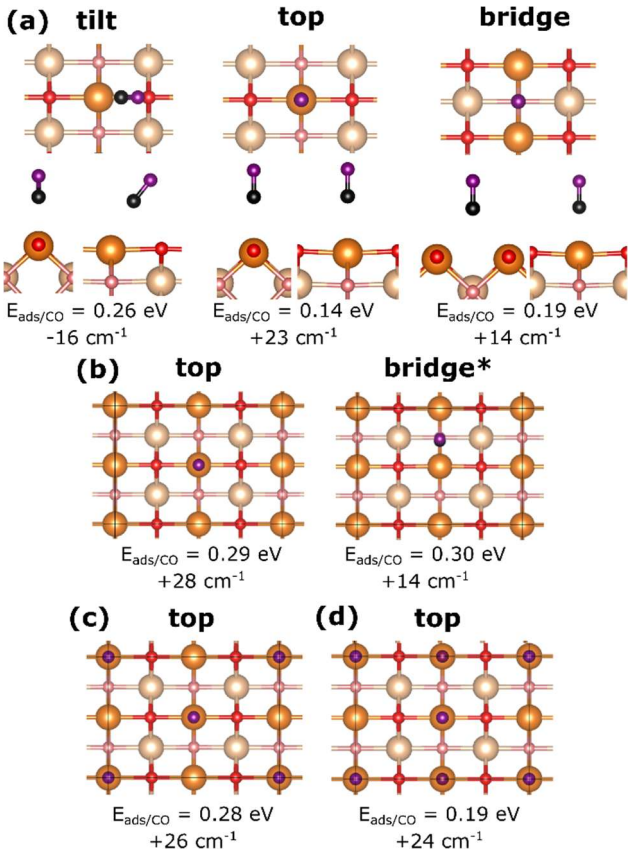

Figure 5. Optimized adsorption geometries (top and side views) for the stable local minima obtained at different coverages Θ on MgO(110). (a) At Θ = 1.0 ML, three adsorption motifs are identified: tilt, top, and bridge configurations. (b) At Θ = 0.25 ML, only on-top and a slightly tilted bridge* minimum remain stable. (c,d) At intermediate coverages Θ = 0.50 ML (c) and Θ = 0.75 ML (d), the calculations converge to a single stable on-top configuration.

Having established the microscopic origin of the high-frequency CO band on MgO(100), we now turn to MgO(110), where fourfold-coordinated Mg_{4c} sites are intrinsic to the ideal surface and thus allow a direct assessment of coverage-dependent adsorption motifs. Figure 5 summarizes the coverage dependence of CO adsorption on MgO(110). At full monolayer coverage (Θ = 1 ML), three local minima are obtained: a tilted configuration, an on-top configuration, and a bridge configuration (Figure 5a). The tilted state is the most strongly bound at this coverage (0.26 eV) and exhibits a red shift of the CO stretching frequency by −16 cm^{-1} relative to gas-phase CO. The on-top state is less strongly bound (0.14 eV) and shows a blue shift of +23 cm^{-1}, while the bridge state is intermediate in stability (0.19 eV) and also presents a blue shift of +14 cm^{-1}. Upon decreasing the coverage to Θ = 0.25 ML (Figure 5b), the adsorption landscape simplifies: only an on-top minimum and a slightly tilted bridge* minimum remain stable. The on-top state binds with an adsorption energy of 0.29 eV and yields a blue shift of $\Delta\nu$ = +28 cm^{-1}, whereas the bridge state is nearly isoenergetic (0.30 eV) but displays a smaller blue shift ($\Delta\nu$ = +14 cm^{-1}). Notably, the fully tilted minimum found at Θ = 1 ML is no longer stable at Θ = 0.25 ML. For intermediate coverages, Θ = 0.50 ML (Figure 5c) and Θ = 0.75 ML (Figure 5d), the calculations converge to a single stable motif: on-top adsorption. The corresponding adsorption energies and frequency shifts are 0.28 eV with $\Delta\nu$ = +26 cm^{-1} at Θ = 0.50 ML, and 0.19 eV with $\Delta\nu$ = +24 cm^{-1} at Θ = 0.75 ML. Overall, when a unique stable minimum is obtained, the computed CO stretching frequency for on-top CO at Mg_{4c} sites varies within a narrow window ($\Delta\nu \approx$ +24–28 cm^{-1}), consistent with the experimental assignment of the MgO(110) band (2165–2175 cm^{-1}, Figure 2a) to on-top CO at Mg_{4c} sites and closely matching, within the expected theoretical accuracy, the band attributed experimentally to step sites on MgO(100).

To further assess the intensity distribution of the Mg_{4c}^{2+}- and Mg_{5c}^{2+}-related bands on MgO(110), we performed additional HSE06 calculations for CO adsorbed on a MgO(110)-based microfaceted model exposing both Mg_{4c}^{2+} and Mg_{5c}^{2+} adsorption environments (Figure S10). These calculations show that the enhanced intrinsic CO-stretching intensity is retained for Mg_{4c}^{2+} sites also in the MgO(110)-based model. The Mg_{4c}^{2+}-associated mode dominates the normalized simulated spectrum, whereas the Mg_{5c}^{2+}-related contribution appears as a weaker lower-frequency band. Thus, the dominant p-polarized MgO(110) band is consistent with CO adsorbed in a near-upright geometry at Mg_{4c}^{2+} sites, whereas the Mg_{5c}^{2+} species become prominent in s-polarization because its tilted adsorption geometry gives rise to a larger in-plane component of the transition dipole moment.

3. Conclusions

In summary, we provide an unambiguous spectroscopic identification of CO adsorbed on well-defined MgO(100) and MgO(110) single-crystal surfaces. On MgO(110), the structural distribution of coordination sites is inverted relative to MgO(100). Importantly, the spectroscopic trend is invariant: Mg_{4c} sites consistently bind CO more strongly and exhibit higher-frequency bands than Mg_{5c} sites, independent of whether they are located at terraces or steps. Notably, while the frequency trend follows coordination, the adsorption geometry depends on surface topology. On MgO(100), CO at Mg_{4c} step-edge sites adopts a tilted configuration, whereas on MgO(110) CO at terrace Mg_{4c} sites is near-upright. Thus, coordination governs adsorption strength and vibrational response, whereas geometric constraints imposed by the surface determine the preferred molecular orientation.

By combining polarization-resolved IRRAS with hybrid HSE06 density functional theory calculations and controlled variation of surface defect populations, we establish site-specific vibrational fingerprints, adsorption geometries, and binding energies for CO on both non-polar, low-index MgO surfaces. Our results demonstrate that reduced coordination at extended step edges profoundly reshapes the local electrostatic environment of an otherwise nonreducible ionic oxide. Calculations of the infrared intensities further show that species bound to low-coordination sites can dominate the IRRAS response even at modest concentrations due to their enhanced transition dipole moments, providing a framework for interpreting vibrational spectra of oxide surfaces where minority structural motifs disproportionately influence spectroscopic signals.

By reconciling adsorption energetics, polarization-resolved vibrational fingerprints, coverage-dependent behavior, and defect thermodynamics within a unified experimental–theoretical framework, these findings resolve a long-standing ambiguity in the CO/MgO literature. More broadly, they highlight coordination-specific engineering of oxide surfaces as a powerful strategy to control adsorption, reactivity, and metal stabilization on wide-band-gap oxide surfaces, with direct implications for defect-engineered materials and oxide-supported single-atom catalysis.

Supporting Information

Supporting information for this article is given via a link at the end of the document. The DFT data that support the findings of this study are available in Materials Cloud (https://www.materialscloud.org/home) with the identifier DOI: 10.24435/materialscloud:XXXXXX

Notes

The authors declare no competing financial interests.

ACKNOWLEDGMENTS

This work was funded by the Deutsche Forschungsgemeinschaft (DFG, German Research Foundation) – Project-ID 426888090 – SFB 1441. W.L. is grateful for PhD fellowships donated by the China Scholarship Council (CSC). Support from the Helmholtz Association is also gratefully acknowledged. PGL and MVGP gratefully acknowledge funding from projects PID2021-128915NB-I00, and PID2024-162810NB-I00 financed by Ministerio de Ciencia, Innovación y Universidades, and ERDF, EU. Computational resources were provided by the Red Española de Supercomputación (RES) at MareNostrum 5 (BSC, Barcelona).

REFERENCES

[1] a) J. W. He, C. A. Estrada, J. S. Corneille, M. C. Wu, D. W. Goodman, *Surf. Sci.* **1992**, *261*, 164-170; b) G. Pacchioni, G. Cogliandro, P. S. Bagus, *Int. J. Quantum Chem.* **1992**, *42*, 1115-1139; c) B. X. Shi, A. Zen, V. Kapil, P. R. Nagy, A. Grüneis, A. Michaelides, *J. Am. Chem. Soc.* **2023**, *145*, 25372-25381; d) G. Pacchioni, T. Minerva, P. S. Bagus, *Surf. Sci.* **1992**, *275*, 450-458; e) G. Pacchioni, K. M. Neyman, N. Rosch, *J. Electron Spectrosc. Relat. Phenom.* **1994**, *69*, 13-21; f) J. Heidberg, M. Kandel, D. Meine, U. Wildt, *Surf. Sci.* **1995**, *331*, 1467-1472; g) G. Spoto, E. Gribov, A. Damin, G. Ricchiardi, A. Zecchina, *Surf. Sci.* **2003**, *540*, L605-L610; h) M. Sterrer, T. Risse, H. J. Freund, *Surf. Sci.* **2005**, *596*, 222-228; i) M. Sterrer, T. Risse, H. J. Freund, *Appl. Catal. Gen.* **2006**, *307*, 58-61; j) C. Chizallet, G. Costentin, M. Che, F. Delbecq, P. Sautet, *J. Am. Chem. Soc.* **2007**, *129*, 6442-6452; k) R. Gerlach, A. Glebov, G. Lange, J. P. Toennies, H. Weiss, *Surf. Sci.* **1995**, *331*, 1490-1495; l) F. Illas, G. Pacchioni, A. Pelmenschikov, L. G. M. Pettersson, R. Dovesi, C. Pisani, K. M. Neyman, N. Rösch, *Chem. Phys. Lett.* **1999**, *306*, 202-204; m) R. Soave, G. Pacchioni, *Chem. Phys. Lett.* **2000**, *320*, 345-351; n) Z. Dohnálek, G. A. Kimmel, S. A. Joyce, P. Ayotte, R. S. Smith, B. D. Kay, *J. Phys. Chem. B* **2001**, *105*, 3747-3751; o) G. Spoto, E. N. Gribov, G. Ricchiardi, A. Damin, D. Scarano, S. Bordiga, C. Lamberti, A. Zecchina, *Prog. Surf. Sci.* **2004**, *76*, 71-146; p) H. J. Freund, G. Pacchioni, *Chem. Soc. Rev.* **2008**, *37*, 2224-2242; q) A. D. Boese, J. Sauer, *Phys. Chem. Chem. Phys.* **2013**, *15*, 16481-16493; r) H. Z. Ye, T. C. Berkelbach, *Faraday Discuss.* **2024**, *254*, 628-640; s) D. P. Woodruff, *Chem. Rev.* **2013**, *113*, 3863-3886; t) C. Di Valentin, G. Pacchioni, *Acc. Chem. Res.* **2014**, *47*, 3233-3241; u) A. Gonchar, J. Lian, T. Risse, H. J. Freund, C. Di Valentin, G. Pacchioni, *Top. Catal.* **2015**, *58*, 811-823; v) J. Sauer, *Acc. Chem. Res.* **2019**, *52*, 3502-3510; w) A. Mitra, M. R. Hermes, M. S. Cho, V. Agarawal, L. Gagliardi, *J. Phys. Chem. Lett.* **2022**, *13*, 7483-7489.

[2] M. A. Aramendia, V. Borau, C. Jimenez, J. M. Marinas, A. Porras, F. J. Urbano, *J. Catal.* **1996**, *161*, 829-838.

[3] M. Glinski, *Appl. Catal. Gen.* **2008**, *349*, 133-139.

[4] a) C. Di Valentin, A. Del Vitto, G. Pacchioni, S. Abbet, A. S. Wörz, K. Judai, U. Heiz, *J. Phys. Chem. B* **2002**, *106*, 11961-11969; b) M. A. Brown, Y. Fujimori, F. Ringleb, X. Shao, F. Stavale, N. Nilius, M. Sterrer, H. J. Freund, *J. Am. Chem. Soc.* **2011**, *133*, 10668-10676; c) R. Schlögl, *Angew. Chem. Int. Ed.* **2015**, *54*, 3465-3520; d) P. Schwach, X. L. Pan, X. H. Bao, *Chem. Rev.* **2017**, *117*, 8497-8520; e) G. A. Mutch, S. Shulda, A. J. McCue, M. J. Menart, C. Ciobanu, C. Ngo, J. A. Anderson, R. M. Richards, D. Vega-Maza, *J. Am. Chem. Soc.* **2018**, *140*, 4736-4742; f) H. H. Fang, S. Wu, T. Ayvali, J. Zheng, J. Fellowes, P. L. Ho, K. C. Leung, A. Large, G. Held, R. Kato, K. Suenaga, Y. I. A. Reyes, H. V. Thang, H. Y. T. Chen, S. C. E. Tsang, *Nat. Commun.* **2023**, *14*; g) S. Zhang, Q. Pessemesse, Z. J. Berkson, A. Van Bavel, A. D. Horton, P. A. Payard, C. Copéret, *Angew. Chem. Int. Ed.* **2023**, *62*; h) S. M. Jin, C. Kwon, A. Bugaev, B. Karakurt, Y. C. Lin, L. Savereide, L. P. Zhong, V. Boureau, O. Safonova, S. Kim, J. S. Luterbacher, *Nat. Catal.* **2024**, *7*, 1199-1212; i) Z. L. Yuan, B. Han, B. Liu, J. Sun, P. Zhou, R. T. Mu, Z. H. Zhang, *Nat. Commun.* **2025**, *16*; j) S. Arndt, G. Laugel, S. Levchenko, R. Horn, M. Baerns, M. Scheffler, R. Schlögl, R. Schomäcker, *Catal. Rev. - Sci. Eng.* **2011**, *53*, 424-514; k) G. Busca, *Chem. Rev.* **2010**, *110*, 2217-2249.

[5] a) M. Chiesa, M. C. Paganini, E. Giamello, C. Di Valentin, G. Pacchioni, *Angew. Chem. Int. Ed.* **2003**, *42*, 1759-1761; b) D. Ricci, C. Di Valentin, G. Pacchioni, P. V. Sushko, A. L. Shluger, E. Giamello, *J. Am. Chem. Soc.* **2003**, *125*, 738-747; c) G. Pacchioni, A. M. Ferrari, *Catal. Today* **1999**, *50*, 533-540; d) E. Florez, P. Fuentealba, F. Mondragón, *Catal. Today* **2008**, *133*, 216-222; e) C. Di Valentin, E. Finazzi, G. Pacchioni, *Surf. Sci.* **2005**, *591*, 70-89; f) A. M. Ferrari, R. Soave, A. D'Ercole, C. Pisani, E. Giamello, G.

Pacchioni, *Surf. Sci.* **2001**, *479*, 83-97; g) M. Sterrer, M. Yulikov, E. Fischbach, M. Heyde, H. P. Rust, G. Pacchioni, T. Risse, H. J. Freund, *Angew. Chem. Int. Ed.* **2006**, *45*, 2630-2632; h) G. Pacchioni, *Chemphyschem* **2003**, *4*, 1041-1047; i) G. Pacchioni, H. Freund, *Chem. Rev.* **2013**, *113*, 4035-4072; j) Y. D. Kim, J. Stultz, D. W. Goodman, *Langmuir* **2002**, *18*, 3999-4004; k) S. Abbet, E. Riedo, H. Brune, U. Heiz, A. M. Ferrari, L. Giordano, G. Pacchioni, *J. Am. Chem. Soc.* **2001**, *123*, 6172-6178; l) G. Pacchioni, *Surf. Rev. Lett.* **2000**, *7*, 277-306.

[6] a) C. Yang, H. Idriss, Y. Wang, C. Wöll, *Acc. Chem. Res.* **2024**, *57*, 3316-3326; b) L. Caulfield, Z. R. Yu, Y. Gu, C. W. Yang, S. Falkner, P. Weidler, M. Schwotzer, C. Feldmann, Y. M. Wang, C. Wöll, *J. Phys. Chem. C* **2025**, *129*, 17643-17652.

[7] a) B. B. Sarma, P. N. Plessow, G. Agostini, P. Concepción, N. Pfänder, L. Q. Kang, F. R. Wang, F. Studt, G. Prieto, *J. Am. Chem. Soc.* **2020**, *142*, 14890-14902; b) S. Abbet, U. Heiz, H. Häkkinen, U. Landman, *Phys. Rev. Lett.* **2001**, *86*, 5950-5953; c) S. Abbet, A. Sanchez, U. Heiz, W. D. Schneider, A. M. Ferrari, G. Pacchioni, N. Rösch, *J. Am. Chem. Soc.* **2000**, *122*, 3453-3457; d) G. Pacchioni, L. Giordano, M. Baistrocchi, *Phys. Rev. Lett.* **2005**, *94*, 226104; e) M. Sterrer, T. Risse, L. Giordano, M. Heyde, N. Nilius, H. P. Rust, G. Pacchioni, H. J. Freund, *Angew. Chem. Int. Ed.* **2007**, *46*, 8703-8706.

[8] L. Marchese, S. Coluccia, G. Martra, A. Zecchina, *Surf. Sci.* **1992**, *269*, 135-140.

[9] O. Robach, G. Renaud, A. Barbier, *Surf. Sci.* **1998**, *401*, 227-235.

[10] C. Yang, W. Wang, A. Nefedov, Y. Wang, T. G. Mayerhöfer, C. Wöll, *Phys. Chem. Chem. Phys.* **2020**, *22*, 17129-17133.

[11] Y. Wang, C. Wöll, *Chem. Soc. Rev.* **2017**, *46*, 1875-1932.

[12] P. A. Redhead, *Vacuum* **1962**, *12*, 203-211.

[13] M. Alessio, D. Usvyat, J. Sauer, *J. Chem. Theory Comput.* **2019**, *15*, 1329-1344.

[14] G. Pacchioni, T. Minerva, *Surface Science* **1992**, *275*, 450-458.

[15] a) M. Buchholz, X. J. Yu, C. W. Yang, S. Heissler, A. Nefedov, Y. M. Wang, C. Wöll, *Surf. Sci.* **2016**, *652*, 247-252; b) S. Chen, P. N. Plessow, Z. R. Yu, E. Sauter, L. Caulfield, A. Nefedov, F. Studt, Y. M. Wang, C. Wöll, *Angew. Chem. Int. Ed.* **2024**, *63*, e202404775.

[16] V. E .Henrich, *Surf. Sci.* **1992**, *57*, 385-392

[17] a) P. Ugliengo, A. Damin, *Chem Phys Lett* **2002**, *366*, 683-690; b) B. Civalleri, L. Maschio, P. Ugliengo, C. M. Zicovich-Wilson, *Phys. Chem. Chem. Phys.* **2010**, *12*, 6382-6386.

[18] A. Zhu, P. Komonvasee, A. Nejad, D. P. Tew, *arXiv preprint arXiv:2512.23879* **2025**.

[19] a) P. G. Lustemberg, P. N. Plessow, Y. Wang, C. Yang, A. Nefedov, F. Studt, C. Wöll, M. V. Ganduglia-Pirovano, *Phys. Rev. Lett.* **2020**, *125*, 256101; b) P. G. Lustemberg, C. Yang, Y. Wang, C. Wöll, M. V. Ganduglia-Pirovano, *J. Chem. Phys.* **2023**, *159*, 034704; c) P. G. Lustemberg, C. W. Yang, Y. M. Wang, M. V. Ganduglia-Pirovano, C. Wöll, *J. Am. Chem. Soc.* **2025**, *147*, 6958-6965.

[20] J. Maul, G. Spoto, L. Mino, A. Erba, *Phys. Chem. Chem. Phys.* **2019**, *21*, 26279-26283.